Journal Title
XX(X):1–15

DOI: 10.1177/ToBeAssigned
www.sagepub.com/
SAGE

Long-Term Guided Wave Structural Health Monitoring in an Uncontrolled Environment through Long Short-Term Principal Component Analysis

Kang Yang[1], Sungwon Kim[2], Rongting Yue[3], Haotian Yue[1], Joel B. Harley[1]

Abstract

Environmental effects are a significant challenge in guided wave structural health monitoring systems. These effects distort signals and increase the likelihood of false alarms. Many research papers have studied mitigation strategies for common variations in guided wave datasets reproducible in a lab, such as temperature and stress. There are fewer studies and strategies for detecting damage under more unpredictable outdoor conditions. This paper proposes a long short-term PCA reconstruction method to detect synthetic damage under highly variational environments, like precipitation, freeze, and other conditions. The method does not require any temperature or other compensation methods and is tested by approximately seven million guided wave measurements collected over two years. Results show that our method achieves an AUC score of near 0.95 when detecting synthetic damage under highly variable environmental conditions.

Keywords

Structural health monitoring, guided waves, big data, principal component analysis, environmental conditions

Introduction

Ultrasonic guided waves are widely studied for structural health monitoring due to their ability to travel long distances with little attenuation[1]. They are also sensitive to structural changes, such as those arising from damage or defects[2–4]. Yet, ultrasonic guided waves are not only sensitive to structural variations but are also easily affected by benign changes in the environment and operation of the structure[5,6]. To process large SHM data sets, these variations need to be identified. Research strategies have primarily addressed relatively small variations, such as temperature[1,7–10]. Less work has focused on large variations from freezing conditions, rain, surface wetting, and other variations. Detecting these conditions is not straightforward. Weather reports are not reliable due to spatial variability in weather. Local measurements of temperature, humidity, and brightness cannot identify all conditions, such as surface wetting from precipitation. If not considered, these effects can cause false alarms and corrupt data used to train machine learning systems.

We divide these variations into four types based on their severity and duration. These four types are (1) small, transient variations, (2) large, transient variations, (3) small, permanent variations, and (4) large, permanent variations.

Four Types of Variations in Guided Wave Data

Type-1 variations (small, transient) generally represent mild or gradual environmental and/or operational changes. For example, a mild environmental variation, like temperature[7,11,12] or humidity[13], or a mild operational variation, like pressure and flow rate[14], can change the shape of ultrasonic guided waves and cause false alarms when detecting real damage or defects on the structure. The effect is transient because when a variation, like a temperature, returns to a reference value, the guided ultrasonic wave's shape will return close to the corresponding baseline guided wave. There has been an abundance of work on understanding and eliminating the influence of type-1 variations from ultrasonic guided waves. Much of this work has focused on addressing temperature variations. Several methods, such as optimal baseline selection[8,15], baseline signal stretch (BSS)[1,7,16], physics-based modeling[17], and other data-driven models citefendzi2016data, Zoubi2021-at,Mariani2020-ih have been created to compensate for temperature variations. Other researchers have used principal component analysis (PCA)[5], genetic algorithms[18], ensemble classification[9], Gaussian mixture models[19], neural network[20], and other machine learning approaches to detect damage directly under temperature variations. However, compensating for other environmental factors (e.g., humidity, brightness, pressure) or detecting damage under these conditions is less commonly addressed since they are less well understood.

[1]Department of Electrical and Computer Engineering, University of Florida, Gainesville, FL, 32608.
[2]Department of Mechanical Engineering, University of Utah, Salt Lake City, UT, 84112.
[3]Department of Electrical and Computer Engineering, University of Connecticut, Storrs, CT, 06269.

Corresponding author:
Joel B. Harley, Department of Electrical and Computer Engineering, University of Florida, Gainesville, FL, 32608.
Email: joel.harley@ufl.edu

Type-2 variations (large, transient) represent dramatic environmental and operational changes, such as caused by heavy rain flooding a railway[21], strong winds blowing a bridge[22], overloaded trucks running on a bridge[23], or ice accumulating on a wind blade[24]. Since type-2 variations change guided waves dramatically, they are often difficult to be distinguished from permanent variations (e.g., damage or defects) over periods ranging from hours (e.g., rain) to weeks (e.g., snow and ice). This leads to false alarms in damage detection algorithms. Papers[24,25] have investigated guided wave changes to detect the existence of ice. However, due to their complexity, there are fewer studies on most other type-2 variations in guided wave data.

Type-3 variations (small, permanent) and type-4 variations (large, permanent) represent damage or defects on a structure, or irreversible changes on a structural health monitoring SHM system. The severity of damage or defects distinguishes the two variations. Type-3 variations represent small structural variations, like microcracks or fatigue in a bridge cable that cannot be readily identified, or small irreversible changes on an SHM system, like hardening of adhesive. These variations may grow gradually over time and become type-4 variations. Type-4 variations represent large, critical cracks or a crash of an SHM system, like a severe degradation of sensors. Vibration-based damage identification methods[26–30] use natural frequencies, phase, mode shapes, and mode curvature to identify variations corresponding to damage in a structure. Due to the rapid development of computation resources and the accumulation of huge datasets, many data-driven methods, such as neural networks[31,32], evolutionary algorithms[33], ensemble learning[9], and statistical methods[34,35] have also been applied to damage detection. Some existing damage detection work identifies damage in the presence of variable temperature[5,9,18,19], loading[14,36], traffic flow[37–39], and wind conditions[40]. Many structural health monitoring papers focus on detecting type-4 variations since they can be identified in a controlled laboratory environment. Type-3 variations are still difficult to detect since they generally appear in the early stages of damage, change guided waves slightly, and are easily hidden by type-1 and type-2 environmental and operational variations.

Distinguishing Type-2 and Type-3/4 Variations

This paper distinguishes type-2 and type-3/4 variations in realistic, highly variable environments. We assume:

1. Type-1 variations are weak in amplitude and correlated over short periods of time (e.g., an hour).
2. Type-2 variations are strong in amplitude but weakly correlated over time due to noisy behavior.
3. The type-3/4 (damage/flaws) variations can be weak or strong in amplitude but are highly correlated over long periods of time (e.g., days, weeks, months).

Leveraging these assumptions, we design a long short-term principal component analysis reconstruction methodology to detect, classify, and distinguish type-2 and type-3/4 variations in the presence of type-1 variations.

Existing papers in the literature[5,34,41] have used principal component analysis (PCA) to map damage variations (type-3/4 variations) to principal components. These principal components are usually extracted from all of the data in a guided wave data set. This is impractical for three reasons. First, these methods often assume specific damage knowledge, such as the principal component containing damage information or the pattern (i.e., a step function) created by the damage in the data.

Second, these methods are not robust to type-2 variations. Type-2 variations will distort guided waves and cause false alarms and be mistaken for damage. Thus, we need to automatically detect and remove type-2 variations[24] to reduce false alarms. Third, this requires a huge amount of processing and computation time for large, multi-years datasets.

Our approach makes two important changes relative to existing strategies. First, rather than finding components with type-3/4 variations, we focus on reconstructing data. This removes the need for prior damage information. Second, we consider principal components over local regions of time (e.g., from hours to weeks). This reduces the computational costs and allows us to highlight differences across time scales. In short-term and long-term periods, type-1 variations will be reconstructed. In the short-term and long-term time periods, type-2 variations (which are noisy and highly variable) will not be effectively reconstructed. Type-3/4 variations will be reconstructed effectively in short-term periods but poorly reconstructed in long-term periods. This is because the weak, but long-term, changes from damage are not well observed in short time windows. Hence, we will distinguish type-3/4 variations from type-2 variations by the difference in long-term and short-term PCA reconstructions. We refer to this as long short-term PCA.

We apply our approach to guided wave data collected continuously at the University of Utah from over two years. This includes data from every season and weather conditions in that region. Guided waves along with temperature, humidity, and brightness have been collected from March 2018 to March 2020 in a natural outdoor environment. Temperature ranges from $-11.4°$C to $52.9°$C. Humidity ranges from 0.7% to 100%. The unit of brightness is lux and the log base 10 of brightness ranges from -3.5 to 6.6 (after taking the log base 10 to the original brightness). Results demonstrate that reconstruction coefficients can be used to both identify and separate regions with synthetically generated damage from regions with type-2 variations.

Methodology: PCA Based Reconstruction

This paper applies a long short-term principal component analysis (PCA) reconstruction method to classify highly variational environments (type-2 variations) and irreversible changes (type-3/4 variations), like damage from natural environments (type-1 variations). The foundation of our method assumes that the first several principal components can linearly reconstruct guided waves from type-1 variations.

We use the first several principal components from PCA to reconstruct a period of guided waves and then calculate correlation coefficients between the original and reconstructed guided waves. We refer to this process as a temporally local PCA algorithm in the paper. The algorithm is shown in Fig. 1. We refer to these correlation coefficients as reconstruction coefficients to distinguish our approach

from damage detection methods that compute the correlation coefficient between the data and a baseline signal.

Periods of time with only type-1 variations will have reconstruction coefficients close to 1. For a short-term window (e.g., across several hours), type-2 variations should have low reconstruction coefficients while type-3/4 variations should have high reconstruction coefficients. For a long-term window (e.g., across several days), type-2 and type-3/4 variations should have low reconstruction coefficients. Based on these differences, we can classify type-1, type-2, and type-3/4 variations, illustrated in Table 1.

Temporally Local Short-Term PCA Algorithm

In this paper, vectors are represented by lower case bold letters such as $\mathbf{x}$. Matrices are represented by uppercase bold letters, such as $\mathbf{X}$. All vectors in the paper are column vectors and $(\cdot)^T$ stands for the transpose of a vector or a matrix. For example, $\mathbf{x}$ is a column vector and is a $\mathbf{x}^T$ row vector.

To perform our algorithm, we consider an ultrasonic guided wave dataset $\mathbf{X}$ containing N measurements. Each measurement contains M samples. We can represent this dataset as a matrix

$$\mathbf{X} = \begin{bmatrix}\mathbf{x}_1 & \mathbf{x}_2 & \dots & \mathbf{x}_N\end{bmatrix}^T , \quad (1)$$

where $\mathbf{x}_i = \begin{bmatrix}x_{i1} & x_{i2} & \dots & x_{iM}\end{bmatrix}^T$ represents a single measurement. We separate the data into local batches, or time windows, of L measurements, as shown in Fig. 1. There is no overlap in measurements between batches. Hence, the $N \times M$ data matrix $\mathbf{X}$ (containing about 700-days measurements) is divided into roughly 350 data batches if the batch size/time window L is 2 days. Batch t of the guided wave dataset $\mathbf{X}_t$ with a batch size L is therefore defined as

$$\mathbf{X}_t = \begin{bmatrix}\mathbf{x}_{tL+1} & \mathbf{x}_{tL+2} & \dots & \mathbf{x}_{tL+L}\end{bmatrix}^T , \quad (2)$$

where $t \in \{0, 1, 2, \dots, N/L\}$. We then use PCA to decompose and reconstruct each guided ultrasonic wave batch. The process of calculating reconstruction coefficients based on PCA can be expressed through five steps.

First, we remove the column mean in the batch $\mathbf{X}_t$ (each column in $\mathbf{X}_t$ subtracts its corresponding column mean) such that the column-wise means in the updated matrix $\widehat{\mathbf{X}}_t$ are zeros.

$$\widehat{\mathbf{X}}_t = \begin{bmatrix}\widehat{\mathbf{x}}_{tL+1} & \widehat{\mathbf{x}}_{tL+2} & \dots & \widehat{\mathbf{x}}_{tL+L}\end{bmatrix}^T \quad (3)$$

$$\widehat{\mathbf{x}}_{tL+i} = \mathbf{x}_{tL+i} - \overline{\mathbf{x}}_t , \quad (4)$$

where $i \in \{1, 2, \dots, L\}$ and $\overline{\mathbf{x}}_t = \frac{1}{L}\sum_{j=1}^{L} \mathbf{x}_{tL+j}$. Both dimensions of $\mathbf{x}_{tL+i}$ and $\overline{\mathbf{x}}_t$ are $M \times 1$. $\overline{\mathbf{x}}_t$ is the vector containing the mean of each column in the matrix $\mathbf{X}_t$ with a dimension of $L \times M$(the mean of each sample in a batch of guided waves $\mathbf{X}_t$). In Eq. 4, each sample in the $tL + i$ measurement $\mathbf{x}_{tL+i}$ will be subtracted by the corresponding sample's mean.

Second, we obtain principal components by computing the eigenvectors of the covariance matrix $\widehat{\mathbf{X}}_t^T\widehat{\mathbf{X}}_t$ for the t batch $\widehat{\mathbf{X}}_t$ according to

$$\widehat{\mathbf{X}}_t^T\widehat{\mathbf{X}}_t\mathbf{v}_{tP+i} = \lambda_{tP+i}\mathbf{v}_{tP+i} , \quad (5)$$

where $\mathbf{v}_{tP+i}$ is a vector of length M. We let $\mathbf{V}_t = \begin{bmatrix}\mathbf{v}_{tP+1} & \mathbf{v}_{tP+2} & \dots & \mathbf{v}_{tP+P}\end{bmatrix}^T$ be an principal component matrix for batch t consisting P principal components that correspond to the P largest eigenvalues of the covariance matrix. The dimension of $\mathbf{V}_t$ is $P \times M$.

Third, we implement an orthogonal projection of our data onto the space of the top P principal components by multiplying the t-th batch $\mathbf{X}_t$ with the principal component matrix $\mathbf{V}_t$ to obtain $\mathbf{Z}_t$ in the projected space,

$$\mathbf{Z}_t = \widehat{\mathbf{X}}_t\mathbf{V}_t^T = \begin{bmatrix}\mathbf{z}_{tL+1} & \mathbf{z}_{tL+2} & \cdots & \mathbf{z}_{tL+L}\end{bmatrix}^T . \quad (6)$$

where the dimension of $\mathbf{Z}_t$ is $L \times P$.

Fourth, a reconstructed guided wave data $\mathbf{X}'_t$ is obtained by the matrix multiplication of $\mathbf{V}_t$ and $\mathbf{Z}_t$, according to

$$\mathbf{X}'_t = \mathbf{Z}_t\mathbf{V}_t + \begin{bmatrix}\overline{\mathbf{x}}_t & \overline{\mathbf{x}}_t & \dots & \overline{\mathbf{x}}_t\end{bmatrix}_{1\times L}^T , \quad (7)$$

where the dimension of $\mathbf{X}'_t$ is $L \times M$.

Table 1. The classification of Type-1, Type-2, and Type-3/4 Variations Based on Long Short-Term PCA Reconstruction.

Long-term reconstruction \ Short-term reconstruction	High	Low
High	Type-1 variation	None
Low	Type-3/4 variation	Type-2 variation

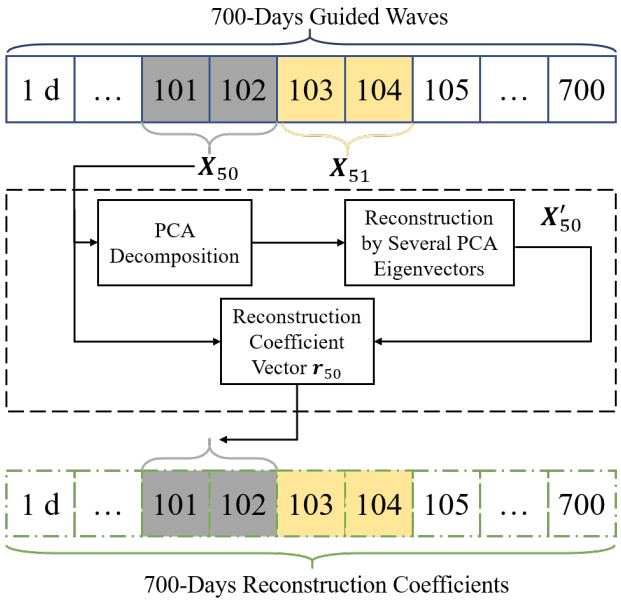

Figure 1. The temporally local PCA algorithm diagram for reconstruction coefficient calculation. In this illustration, we assume the short-batch size is 2 days and the stride 2-days (hence, there is no overlap between the 50-th batch data X_{50} and the 51-th batch data X_{51}). The diagram is calculating the reconstruction coefficients of the 50-th (the 101 and 102 day) guided waves X_{50}.

Finally, the reconstruction coefficients of guided waves in $\mathbf{X}_t$ are calculated according to

$$r_{tL+i} = \frac{\left(\mathbf{x}'_{tL+i} - \overline{x}'_{tL+i}\right)^T \left(\mathbf{x}_{tL+i} - \overline{x}_{tL+i}\right)}{\|\mathbf{x}'_{tL+i} - \overline{x}'_{tL+i}\| \|\mathbf{x}_{tL+i} - \overline{x}_{tL+i}\|} \quad (8)$$

$$\overline{x}_{tL+i} = \frac{1}{M}\sum_{j=1}^{M} x_{tL+i,j} \quad (9)$$

$$\overline{x}'_{tL+i} = \frac{1}{M}\sum_{j=1}^{M} x'_{tL+i,j} \quad (10)$$

where $t \in \{0, 1, 2, \ldots, N/L\}$, $i \in \{1, 2, \ldots, L\}$, and $\|\cdot\|$ represent the Euclidean norm. The dimension of $\mathbf{x}_{tL+i}$ and $\mathbf{x}'_{tL+i}$ are $M \times 1$. $\overline{x}_{tL+i}$ and $\overline{x}'_{tL+i}$ are two scalars, representing the mean of all samples/features in the guided wave $\mathbf{x}_{tL+i}$ and the reconstructed guided wave $\mathbf{x}'_{tL+i}$. The reconstruction coefficients $\mathbf{r} = \begin{bmatrix} r_1 & r_2 & \ldots & r_N \end{bmatrix}^T$ are the core metrics we use to distinguish each of the different variations.

Temporally Local Long-Term PCA Algorithm

Long-term PCA reconstruction uses the same approach as our short-term PCA reconstruction algorithm but has a different batch size and nearby long-term batches of guided waves are partly overlapped. In the short-term PCA reconstruction, guided waves from nearby batches are not overlapped and each reconstruction coefficient from a short-term batch L_{short} will be saved. In the long-term PCA reconstruction, the batch size L_{long} is significantly longer than L_{short} and we only compute the reconstruction coefficient for the final L_{stride} measurements. L_{stride} is the stride size of the long-term PCA time window.

For this paper, we will use a long-term batch size L_{long} of 10 days and a short-term batch size L_{short} of 1 day. The stride size of long-term PCA time window L_{stride} is set to 1 day. This means 9 days of guided waves from two nearby batch will be overlapped in the long-term PCA reconstruction, shown in Fig 2. Note that if the damage is stationary (not changing over time), the long-term reconstruction coefficient will return to a high condition when L_{long} length window is fully contained in the data with damage. Fig 2 illustrates how our short-term PCA and long-term PCA are implemented.

Damage Detection

Damage (i.e., a long-term anomaly in the data) is detected from the difference between the short-term and long-term PCA reconstruction coefficients, defined by

$$dr_{tL+i} = \frac{r^{(S)}_{tL+i}}{r^{(S)}_{t,median}} - \frac{r^{(L)}_{tL+i}}{r^{(L)}_{t,median}} \quad (11)$$

where $r^{(S)}_{tL+i}$ and $r^{(L)}_{tL+i}$ are the short-term and long-term PCA reconstruction coefficients, respectively. The terms,$r^{(S)}_{t,median}$ and $r^{(L)}_{t,median}$ are the medians of the corresponding short-term and long-term batches. These normalizations reduce drift in the reconstruction coefficients over time, which varies with the amount of random noise in the data. We use the median rather than the mean since the median will be robust to spurious outliers. When the short-term and long-term normalized PCA reconstruction coefficients observe no variations, $dr_{tL+i} \approx 0$. When the normalized long-term reconstruction coefficients are smaller than the normalized short-term reconstruction coefficients, then the data may contain damage.

To avoid the false alarms from highly variational environment, we set dr_{tL+i} to 0 for measurements from type-2 variations. We identity type-2 variations such that (λ is a user chosen threshold. Here we set λ to 0.99)

$$r^{(S)}_{tL+i} \leq \lambda \quad (12)$$

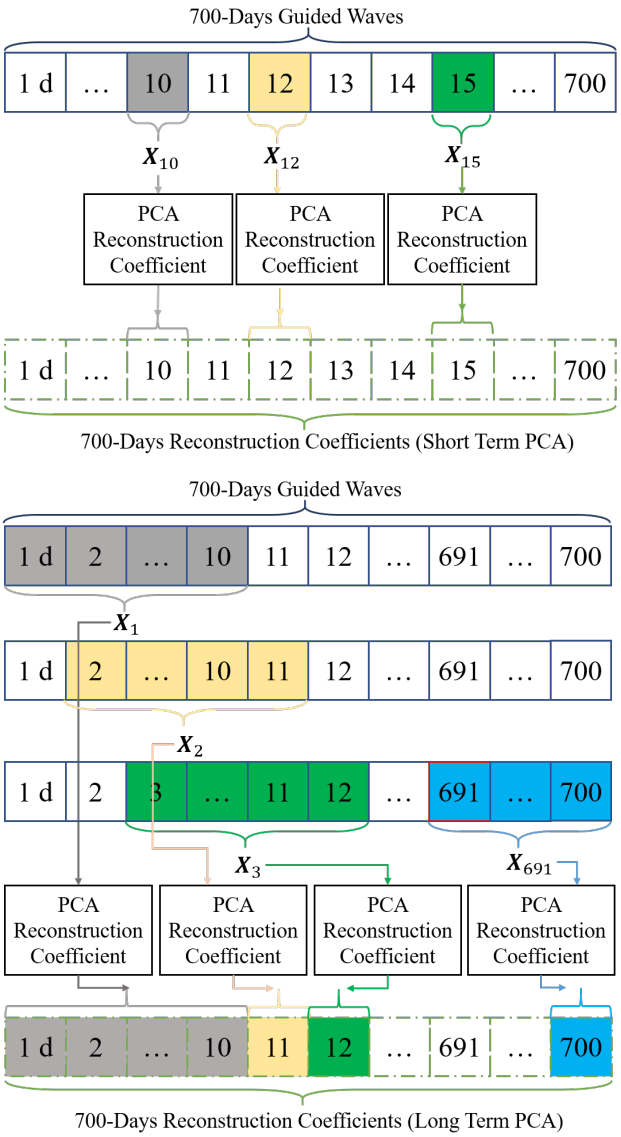

Figure 2. The short-term and long-term PCA reconstruction coefficients calculation process. In the short-term PCA reconstruction, the time window is 1 day and stride size is 1 day (e.g., there is no overlap between the 10-th batch data X_{10} and the 11-th batch data X_{11}). In the long-term PCA reconstruction, the batch size/time window L_{long} contains 10-days of guided waves and the stride size is 1 day. After obtaining the reconstruction coefficients for the 2nd batch data (X_2), reconstruction coefficients of the 11-th day guided waves are appended into the result and reconstruction coefficients from the 1st to the 10th remain unchanged.

Therefore, we identify damage at measurements such that

$$dr_{tL+i} \leq \eta \tag{13}$$

where η is a user chosen threshold. Note that to further reduce the effects of spurious outliers, we also apply a 3-hour long running median filter to dr_{tL+i} before applying the threshold. This step improves detection performance (AUC score) by about 3% to 4% in our results.

We use true positive rate (TPR) and false positive rate (FPR) to evaluate the performance of our method. The true positive rate is defined by

$$TPR = \frac{TP}{TP + FN} \tag{14}$$

where TP is the number of true positives (the number of measurements correctly identified as possessing from synthetic damage) and FN is the number of false negatives (the number of measurements with synthetic damage that were missed). The false positive rate is defined by

$$FPR = \frac{FP}{TN + FP} \tag{15}$$

where FP is the number of false positives (the number of measurements incorrectly identified as possessing synthetic damage) and TN is the number of true negatives (the number of measurements correctly identified as benign conditions). The plot of TPR to FPR is known as the receiver operating characteristics (ROC) curve. We use the area under the ROC curve (AUC) as our ultimate metric of performance.

Experimental Setup

We apply our approach to an experiment that has been running at the University of Utah, Salt Lake City, since March 2018[42]. The experimental setup consists of a 53 cm by 53 cm aluminum plate with a 3mm thickness, a data acquisition system, 8 ultrasonic transducers, and 4 environment sensors for measuring temperature, humidity, brightness, and air pressure. The system is designed to monitor the status of the aluminum plate under many kinds of natural conditions. The equipment is placed in a small room with 4 walls but no roof and is exposed to an outdoor environment under natural conditions. The environment and equipment are shown in Fig. 3.

Ultrasonic guided wave signals are transmitted and collected by ultrasonic transducers, which convert the voltage to mechanical vibration or vice versa. Our sensors are composed of 7 mm diameter by 0.2 mm thick piezoelectric SM412 ceramic discs from StemInc with a 300 kHz radial mode resonance. The sensors are covered in epoxy to provide some layer of protection from the elements. The sensors transmit a chirp signal with frequency from 5 kHz to 350 kHz. Each measurement is taken with a sampling rate of 1 MHz. Among eight ultrasonic transducers, six of them are used to monitor the status of the aluminum plate. Two of the six ultrasonic sensors are used to transmit guided ultrasonic signals, and four of the six ultrasonic sensors are used to collect guided wave signals. Each guided wave consists of 10000 samples. In one measurement, the system will collect 8 ultrasonic guided signals (4 ultrasonic signals from each transmit transducer) and 4 environment values, including temperature humidity, air pressure, and brightness[42,43].

The experimental equipment is placed on a shelf with 2 layers. The plate with 8 ultrasonic transducers is on the first layer. Temperature, humidity, air pressure, and brightness sensors are on the second layer's foam box. Equipment on the first layer is exposed to sunlight, rain, dew, snow, hail, ice, and other conditions directly. Equipment on the second layer is not exposed to these conditions. The temperature and brightness sensors are not entirely covered and observe brief periods of direct sunlight. However, since the sensors are covered, the spurious change is narrower in time than that observed in the reconstruction coefficients.

When collecting our data, each measurement is captured about every 9 seconds. During a measurement, the total measurement time is less than 20 ms. The experiment takes more than 10,000 measurements per day. The experiment has millions of measurements under all kinds of weather, including rain, snow, clouds, wind, and ice. A few different measurement environments are shown in Fig. 4. Note that rain leaves wetting on the plate, snow covers the plate, and ice is converted into surface wetting and vice versa due to temperature variations.

Type-2 Variation Detection Experiment

For this experiment, we study a subset of data that includes approximately seven million measurements (2 years of measurements). Each measurement includes 8 ultrasonic guided waves, a humidity value, a temperature value, an air pressure value, a brightness value, and the time when the measurement was collected. Due to the size of the data set, we only analyze guided waves from the first transmitter sensor (sensor 5) and received by the fourth receiver sensor (sensor 1), shown in Fig. 5. Since the signal decays quickly, we only analyze the first 2000 samples measured (2 ms). We choose a 2 ms length since the synthetic damage has a strong effect on later parts of the data, as evidenced by Fig. 11. Hence, a longer signal length will have a greater sensitivity to damage. It should be noted, however, that a longer signal will also have a greater sensitivity to environmental factors.

We apply a short-term PCA reconstruction method to detect type-2 variations since a short time window will guarantee that the first several components will represent type-1 variations and reconstruct guided waves from type-1 variations better. In the experiment, the time window used to reconstruct guided waves is about one day (the batch size L is $10,000$) since the shortest period of type-1 variations is one day in a natural environment. The slide window step is also 1 day. Thus, there is no overlap between two nearby batches. We will apply the first 15 components to reconstruct $6,942,000$ guided waves $10,000$ by $10,000$. The parameters used by our short-term PCA reconstruction are in Table 2. A histogram of reconstruction coefficients in Fig. 6 shows that most of the signals are reconstructed with high accuracy.

Synthetic Damage Detection Experiment

We did not produce real damage in the experiment implemented at the University of Utah. To test the method's performance in detecting damage, we use the synthetic damage method, shown in paper[43], to generate synthetic

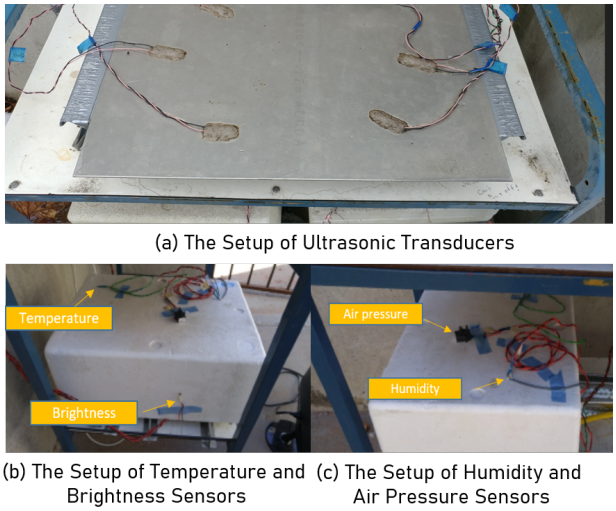

(a) The Setup of Ultrasonic Transducers

(b) The Setup of Temperature and Brightness Sensors

(c) The Setup of Humidity and Air Pressure Sensors

Figure 3. The setup of ultrasonic, temperature, brightness, air pressure and humidity sensors. (a) The top level, containing the ultrasonic sensors and aluminum plate under test. (b) The bottom level, containing the sensors and environmentally protected data acquisition system.

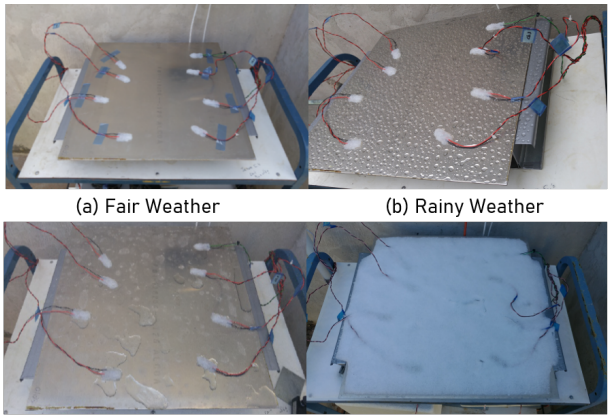

(a) Fair Weather (b) Rainy Weather

(c) Surface Wetting Weather (d) Snow Weather

Figure 4. Various kinds of measurement environments experienced when monitoring the plate's structural health. The conditions in (b),(c), and (d) represent three different type-2 variations.

damage. As mentioned in the paper[43], a guided wave from a damage situation can be approximated by the superposition between a direct guided wave from a transmitter and a subsequent guided wave transmitted by a damage point, shown in Fig. 5.

Thus, we select a guided wave from the shortest signal path (path 5–1) as a pristine signal and select a guided wave from the longest path (path 5–4) as the signal transmitted by a damage point. Typically, the magnitude of a guided wave transmitted by a damage point should be smaller than a pristine guided wave since a damaged guided wave will travel a longer distance and lose energy when being transmitted. Thus, a synthetic damage signal is defined as

$$\widehat{\mathbf{y}}_i = \mathbf{y}_i + \gamma \mathbf{y}'_i \,, \tag{16}$$

where $\mathbf{y}_i$ is the i_{th} guided wave from the path 5–1, $\mathbf{y}'_i$ is the i-th guided wave from the path 5–4, and γ is the scatter factor. In prior work[44], a 10 cm by 10 cm dense wavefield of Lamb waves from a steel plate with a circular 2-mm diameter half-thickness notch at its center. In the experiment, the notch produces a reflection around 0.1 to 0.2 times that of the direct waves. Hence, in this paper, we consider γ values of 0.05, 0.1, and 0.2.

We apply the long short-term PCA reconstruction method to detect synthetic damage moments (type-3/4 variations). The short time window is about one day (the batch size is $10,000$) since the shortest period of type-1 variations is one day in a natural environment. We will use the first 15 components to reconstruct guided waves in the short time window and use the first 15 components to reconstruct guided waves in the long time window. The parameters used by long-term PCA reconstruction are in Table 3.

To test our damage detection performance, we select 30 regions from the measurements and create synthetic damage. We chose 30 regions with diverse weather conditions, including precipitation, surface wetting, direct sunlight, and fair weather. Thus, each region is about 10 days long and with 12 to 36 hours of synthetic damage within it. We expect our method to detect the start of synthetic damage. Considering the stride size of the long-term PCA reconstruction is about 24 hours, it will be reasonable for our method to detect these synthetic damages within the first two strides (48 hours). So, we set the duration of the synthetic damage to vary from 12 hours to 36 hours and begin at a random time within each region. These periods of synthetic damage are generated across many conditions, including precipitation, direct sunlight, freezing conditions, fair weather, etc.

Table 2. Parameters for detecting synthetic damage based on the long short-term PCA reconstruction.

Parameters	Values
Samples M	2000
Short-Term Batch Size L	10,000 ($\approx$ 1 day)
# of Short-Term Principle Comp.	15
# of Total Measurements	6,942,000 ($\approx$ 2 years)

Table 3. Parameters for detecting synthetic damage based on the long short-term PCA reconstruction.

Parameters	Values
Samples M	2000
Short Batch Size L_{short}	10,000 ($\approx$ 1 day)
Long Batch Size L_{long}	100,000 ($\approx$ 10 days)
Stride Size in Long-Term PCA L_{long}	10,000 ($\approx$ 1 days)
# of Short-Term Principle Comp.	15
# of Long-Term Principal Comp.	15
# of Cases with Synthetic Damage	30 (damage cases vary from 12 to 36 hours)
# of Total Measurements	3,000,000 ($\approx$ 10 month)

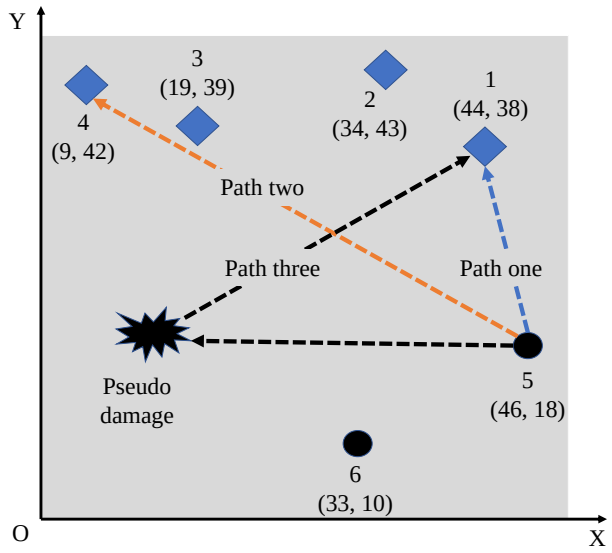

Figure 5. The approximate locations of transmitters and receivers (X:cm Y:cm). A damaged guided wave can be approximated by the superposition of a direct guided wave and a transmitted guide wave from a damage point

.

Effect of Variations on Guided Waves

Figs. 7 to 11 compare the measured, pulse compressed guided waves from different conditions (precipitation, surface wetting, freezing condition, and direct sunlight) with the measured pulse compressed guided waves from fair weather. Note that these figures represent specific example signals. They are not representative of all precipitation, wetting, freezing, or direct sunlight conditions. Fig. 7 and Fig. 8 illustrate the effects of precipitation and the effects of surface wetting on the actual guided wave signals (shown after pulse compression). The measurement times and the reconstruction coefficients for these guided waves are shown in the legend. The reconstruction coefficients of selected guided waves in fair, precipitation, and surface wetting conditions are 0.990, 0.756, and 0.745, respectively. We observe that the magnitude of the actual guided waves from precipitation and surface wetting is smaller and noisier than those from fair weather. The guided waves also vary more rapidly in the precipitation and surface wetting conditions.

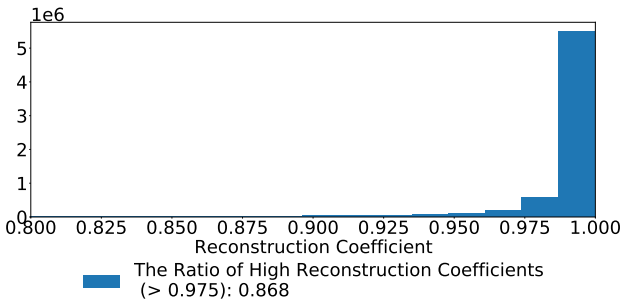

Figure 6. The histogram of reconstruction coefficients of all measurements from the short-term PCA reconstruction (using the first fifteen principal components and the time window is about one-day). Most signals can be reconstructed well since over 86.8% of guided waves can achieve a reconstruction coefficient over 0.975

The actual pulse compressed guided waves from fair and freezing conditions are plotted in Fig. 9. We observe that when the reconstruction coefficient is below 0.5, the guided waves' amplitude is diminished substantially and is almost entirely composed of noise. It is not immediately clear why the data acquisition system fails to collect good guided waves in the freezing condition, but the freezing conditions do not appear to cause permanent changes to the guided waves data since when the temperature goes up, the abnormal measurements disappear. Since it is difficult for PCA to reconstruct signals made of unstructured noise, the reconstruction coefficients for these guided waves are very low.

Fig. 10 illustrates the actual pulse compressed guided waves from fair and direct sunlight conditions. The reconstruction coefficient from fair weather is about 0.989, and the reconstruction coefficient from direct sunlight events is 0.864. Although the reconstruction coefficients are different, the pulse compressed the guided waves from fair and direct solar radiation is not significantly different.

Fig. 11 illustrates actual guided waves from fair, with and without synthetic damage. The reconstruction coefficient without damage is 0.989, and the reconstruction coefficient with synthetic damage is 0.978.The pulse compressed guided wave from synthetic damage is close to that of fair weather. From this, we observe that the synthetic damage has the weakest effect among these different variations.

Results and Discussion

This section will show our method's performance on classifying type-2 variations and type-3/4 variations from within type-1 variations. First, we will show the short-term PCA reconstruction method's effectiveness in detecting type-2 variations – precipitation/surface wetting, direct sunlight, and freezing conditions. We will then show the long short-term PCA reconstruction to detect type-3/4 variations in the presence of type-1 and type-2 variations.

Identifying Predominant Type-2 Variations

We choose the short-term PCA reconstruction method and use the first 15 principal components to decompose and reconstruct guided waves from 2-year measurements. The short-term PCA reconstruction time window is a one-day (batch size is $10,000$). The reconstruction coefficients, along with corresponding temperature, humidity, brightness, and measurement times, are shown in the following results. Most of the reconstruction coefficients in the 2-years guided waves (about 7 million measurements) are close to 1, shown in Fig. 6. Hence, the first fifteen principal components will be enough to represent most one-day type-1 variations in the 2-years guided waves.

The following results study situations in which these reconstruction coefficients drop significantly. We provide significant evidence to support our hypothesis that the drop in the reconstruction coefficients results from type-2 variations. This significant evidence is from the corresponding changes in humidity, temperature, air pressure, brightness, and weather reports. Based on the available data, we focus on four categories of type-2 variations: precipitation, surface wetting, direct sunlight, and freezing conditions.

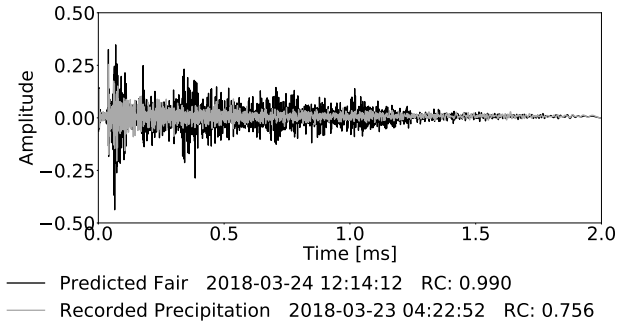

Figure 7. Guided wave signals after pulse compression by the transmitted chirp signal during precipitation and in fair weather. The precipitation causes the guided wave amplitude to decrease and become more noisy.

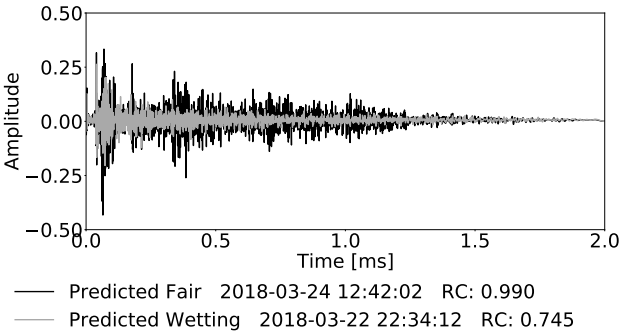

Figure 8. Guided wave signals after pulse compression by the transmitted chirp signal in surface wetting and in fair weather. The surface wetting causes the guided wave amplitude to decrease and become more noisy.

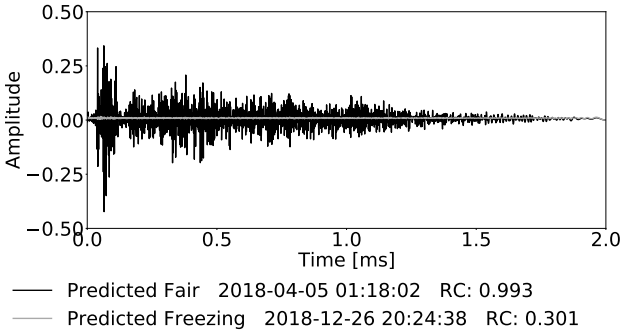

Figure 9. Guided wave signals after pulse compression by the transmitted chirp signal in freezing conditions and in fair weather. The magnitude of a guided wave in freezing weather decrease to almost 0 and is dominated by noise.

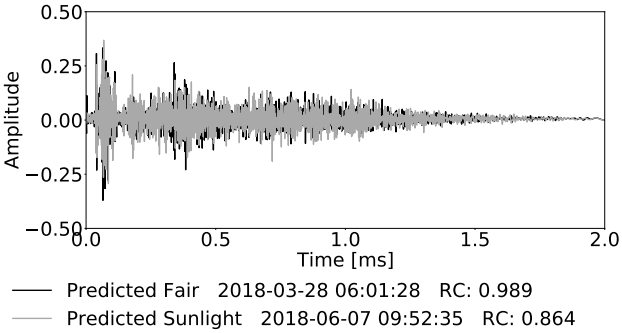

Figure 10. Guided wave signals after pulse compression by the transmitted chirp signal during direct sunlight and in fair weather. There is no obvious differences between these signals. Our method identifies the relatively rapid signal change.

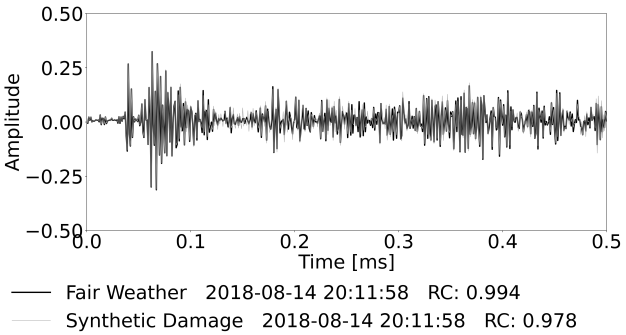

Figure 11. Guided wave signals after pulse compression by the transmitted chirp signal in fair weather, with and without synthetic damage with $\gamma = 0.2$. The plots show the effect of synthetic damage is significantly weaker than that of type-2 variations (the two guided waves are almost overlapped).

Identifying Precipitation and Surface Wetting Based on the times of precipitation events from a public online archive[45], we have found that these precipitation events overlapped with strong drops in the reconstruction coefficient. During these events, we also observe simultaneous increases in humidity, decreases in temperature, and decreases in brightness. These variations are illustrated in Fig. 12, where gray points are unlabeled (i.e., likely representing fair conditions), black points are recorded precipitation events.

During these recorded precipitation events, the reconstruction coefficients will often drop significantly (below 0.8), but sometimes the drop in reconstruction coefficients is smaller. This phenomenon may be caused by variable rainfall intensity around the plate. Strong rainfall intensity is likely to result in a larger drop in the reconstruction coefficient.

Shortly after the recorded precipitation, many reconstruction coefficients remain low but gradually increase to 1. This can be observed in 04-03-2018, 04-07-2018, and 04-08-2018 in Fig. 12. These trends generally occur after high humidity. As a result, we believe this is due to surface wetting when residual water remains on the plate.

While recorded precipitation events are correlated with low reconstruction coefficients, we can identify other potential precipitation events, such as on 04-12-2018 and 04-14-2018. We believe these can be identified as precipitation since the patterns seen among the reconstruction coefficient, temperature, humidity, and brightness are similar to those from recorded precipitation events. Note that the location of the meteorological station is about 15 miles away from the experiment location. Hence, the recorded precipitation events may not completely align with those experienced by the experiment location. Thus, we believe potential precipitation events, such as 04-12-2018, 04-14-2018, and 04-16-2018, are unrecorded precipitation events.

Identifying Freezing Conditions Between November and March, there are many events in which the reconstruction coefficients drop sharply, but precipitation is not observed, as shown in Fig. 13. These drops in the reconstruction coefficients occur when the temperature is cold (typically below 0° C). For example, in Fig. 13, 2019-01-21 to 2019-02-02 shows clear patterns in the reconstruction coefficient

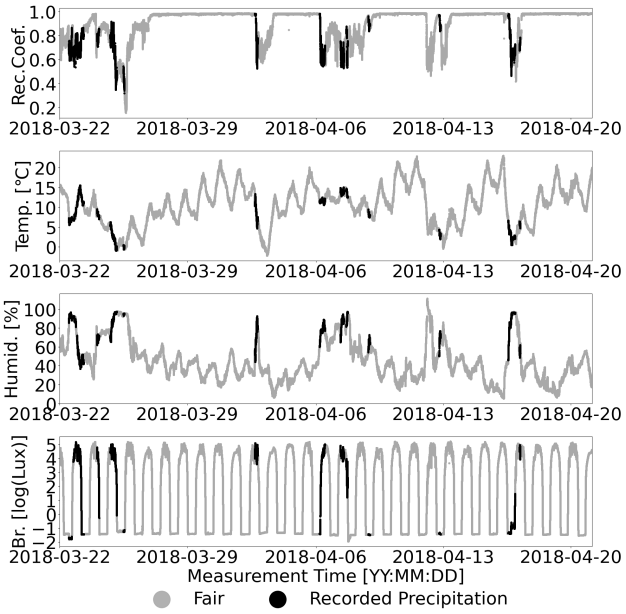

Figure 12. The reconstruction coefficients, temperature, humidity, and brightness in precipitation conditions. In fair weather, reconstruction coefficients of guided waves approach 1 but drop during precipitation. Reconstruction coefficients are from the short-term PCA reconstruction (using the first fifteen principal components and the time window is about one-day)

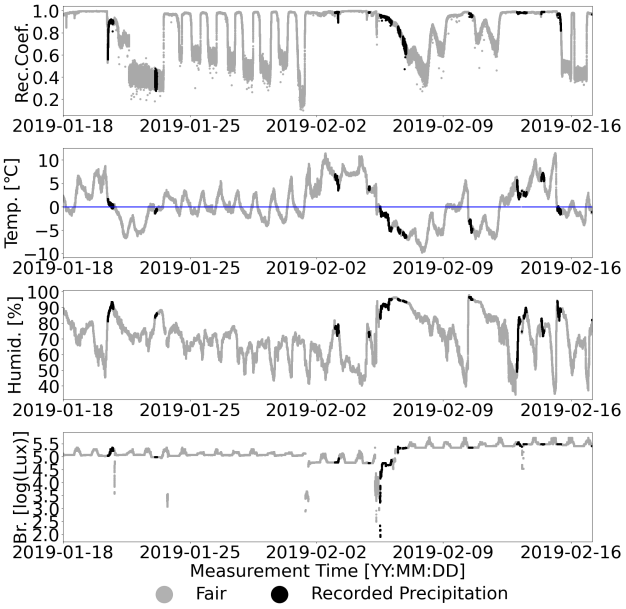

Figure 13. The reconstruction coefficients, temperature, humidity, and brightness in freezing conditions. In fair weather, reconstruction coefficients approach 1 and drop when temperature drops be 0 degrees C. Reconstruction coefficients are from the short-term PCA reconstruction (using the first fifteen principal components and the time window is about one-day).

when the temperature is below zero. The reconstruction coefficient will often drop below 0.5 sharply at these times. When the temperature rises above zero, the reconstruction coefficient will again approach 1.

Identifying Direct Sunlight Around 10 AM for days from May to July, we observe another set of low reconstruction

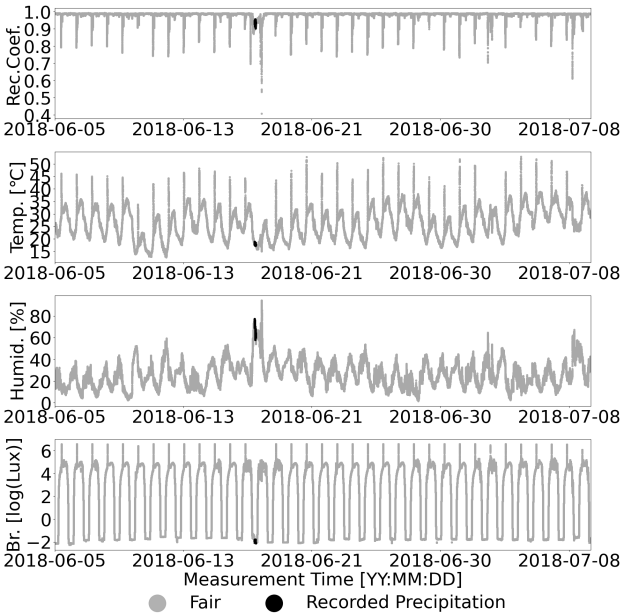

Figure 14. The reconstruction coefficients, temperature, humidity, and brightness around direct sunlight conditions. In fair weather, the reconstruction coefficients approach 1 and drop when brightness and temperature spikes. Reconstruction coefficients are from the short-term PCA reconstruction (using the first fifteen principal components and the time window is about one-day).

coefficients. The drop in reconstruction coefficients is less than that of precipitation and freezing events. Reconstruction coefficients during these events do not drop below 0.8 and occur when humidity is low, brightness is strong, and the temperature is relatively high. These events are illustrated in Fig. 14. We believe these variations correspond to direct sunlight on the plate, causing a rapid change in environmental conditions.

The experiment is implemented at the University of Utah in Salt Lake City. The solar altitude in Salt Lake City will be the largest in the summer solstice, June 20th. Thus, around June 20th, it is most possible for direct sunlight to occur on the plate, which is generally shaded by walls on all four sides. The direct sunlight may make the surface temperature of the plate very high. The high temperature may change the shape of guided waves and thus cause a rapid reduction in the reconstruction coefficient. Thus, we consider direct sunlight, another category of type-2 variation.

Automated Detection of Type-2 Variations

From Figs. 12, 13, and 14, we have identified three categories of type-2 variations – precipitation/surface wetting, freezing conditions, and direct sunlight – these will cause the low reconstruction of guided waves. Based on our empirical observation in Fig. 6, we define a reconstruction coefficient value below 0.975 as a low reconstruction coefficient. In this section, we statistically show that reconstruction coefficient drops obtained from the short-term PCA are caused by type-2 variations.

Detection Performance of Individual Events To demonstrate that our low reconstruction coefficients from the short-term PCA reconstruction correspond to type-2 variations, we

assess the ratio of measurements with low reconstruction coefficients in precipitation, freezing, and direct sunlight conditions, shown in Fig. 15. These type-2 conditions are defined as follows:

- Precipitation conditions are determined based on the recorded archive of precipitation[45].
- Freezing conditions are defined as times when the temperature is below 0.
- Direct sunlight events occur predictably around 10:30 AM between May 15th to July 30th every year. Thus, we define 10 AM to 11 AM from May 15th to July 30th as direct sunlight conditions.

Across all measurements, precipitation, freezing, and direct sunlight conditions consist of 5%, 14%, and 1% of the data, respectively. Most of the data (80%) are considered fair conditions. The ratio of measurements with low reconstruction coefficients is:

$$r_i = \frac{|V_i \cap L|}{|V_i|} , \tag{17}$$

where V_i is the set contains measurements from the i^{th} environment situation and $i \in \{1, 2, 3, 4\}$. 1, 2, 3, and 4 represent precipitation, freezing, direct sunlight, and other situations, respectively. and L is the set of contains all measurements with low reconstruction coefficients. $|\cdot|$ represents the number of elements in a set and "$\cap$" means union operation.

This ratio is statistically known as a method's recall metric, the rate at which a category is correctly predicted by the low reconstruction coefficient. We use recall to measure performance since there may be other type-2 variations (i.e., low reconstruction coefficients unaccounted for in our three categories). For example, we lack surface wetting records. In addition, there are likely occurrences of precipitation that are not accurately recorded or may be shifted in time when compared with data from the remote weather station. This is observable by periods of high humidity and low reconstruction coefficients that are not labeled as precipitation by the data source. This imperfect knowledge of the labels greatly and negatively impacts accuracy but not recall. The recall rate reveals the dependency between type-2 variations and low reconstruction coefficients.

Under these conditions, the recall for precipitation, freezing, and direct sunlight conditions by measurements with low reconstruction coefficients are 35%, 43%, and 47%, respectively. However, the recall for the other times (mostly fair weather conditions) by measurements with low reconstruction coefficients is only 6%, shown in Fig. 15. This demonstrates that a low reconstruction coefficient is most likely to occur at the same time as type-2 variations.

Detection Performance of Clustered Events The previous recall of type-2 variations by measurements with low reconstruction coefficients likely does not perfectly reflect the correlation between low reconstruction coefficients and type-2 variations due to transitory periods, such as periods where precipitation is beginning or ending. Hence, a time difference between real precipitation conditions and recorded precipitation conditions results in an underestimated recall. This is why the ratio of measurements

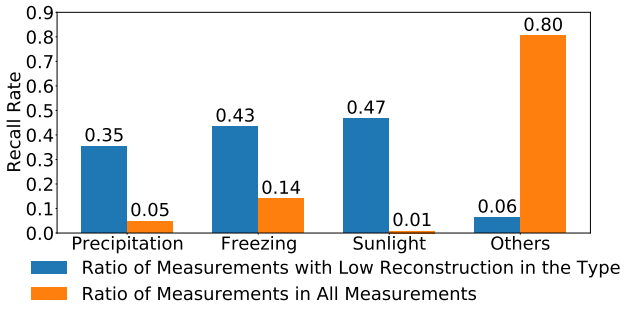

Figure 15. The first bars (blue) describe the ratio of measurements with low reconstruction in each category (i.e., the recall). For example, 35% of measurements collected during precipitation obtain low reconstruction coefficients. The second bars (orange) describe the ratio of each category across all measurements. Hence, measurements from precipitation, freezing condition, direct sunlight, and the other conditions are 5%, 14%, 1%, and 80% of the two years of data, respectively. The sum of these values is 100%.

with low reconstruction coefficients is not high (e.g., 35% on average for precipitation). To eliminate these transitions' influence, we consider the ratio of measurements from clusters of low reconstruction coefficients to measurements from clusters of type-2 variation events. That is, we consider a cluster recall.

In this context, the definitions of precipitation, freezing, direct sunlight, and low reconstruction clusters are:

- A continuous group of measurements from precipitation condition is defined as a precipitation cluster. For example, if the weather history records that precipitation started at 2 AM and ended at 3 AM on April 10, 2018, measurements from 2 AM to 3 AM on April 10, 2018, will be considered as a precipitation cluster.
- A continuous group of measurements whose temperatures are below 0° C is defined as a freezing cluster.
- A continuous group of measurements from 10 am to 11 am each day from May 15th to July 30th is defined as a direct sunlight cluster.
- A continuous group of measurements whose reconstruction coefficients are below 0.975 is defined as a low reconstruction cluster.

Leveraging the definitions of precipitation, freezing, and direct sunlight clusters, we can define the cluster recall of a category of type-2 variation as the ratio of measurements from a category of type-2 variation clusters that overlap with one or more low reconstruction clusters to all measurements from the category of type-2 variation clusters. However, using overlapped low reconstruction clusters and type-2 variation clusters to calculate cluster recalls of type-2 variation conditions may still be restrictive and underestimate the cluster recalls since there may exist time differences between recorded type-2 variations and the true type-2 variations.

There are several reasons why a time difference between recorded conditions and true conditions could occur. First, the 15 miles distance between the meteorological station and the experiment location may cause weather records[45] to be imprecise. For example, there may be a 2 hour time difference between a recorded and true precipitation time.

Hence, a low reconstruction cluster will not overlap with any type-2 clusters and will be 2 hours away from the precipitation cluster. Second, there will likely be a delay between the ambient temperature (which we measure) and our metal plate's temperature. Hence we extend our regions over which overlaps may occur. In this case, we define the cluster recall of the i-th category of type-2 variations $r_i^{(c)}$ as

$$r_i^{(c)} = \frac{|V_i^{(c)} \cap^+ L^{(c)}|^+}{|V_i|^+}, \tag{18}$$

where set $V_i^{(c)}$ contains measurements from the i-th category of type-2 variation clusters, each of which overlaps with or is adjacent to one or more low reconstruction clusters, and set V_i contains all measurements from the i-th category of type-2 variation condition. $i \in \{1, 2, 3\}$ and 1, 2, and 3 represent precipitation, freezing, and direct sunlight situations, respectively. $|\cdot|^+$ represents the number of measurements from specific clusters and "$\cap^+$" means "overlapped with or is adjacent to one or more clusters". Cluster recall $r_i^{(c)}$ can describe how well any of our three type-2 variations condition can be recalled or identified by measurements with low reconstruction coefficients.

Leveraging this idea, we can also use the cluster recall of low reconstruction measurement $r_L^{(c)}$ to demonstrate how many measurements with low reconstruction coefficients are caused by precipitation, surface wetting, freezing, and direct sunlight conditions. We define this cluster recall as

$$r_L^{(c)} = \frac{\left|\left(V_1^{(c)} \cup V_2^{(c)} \cup V_3^{(c)}\right) \cap^+ L^{(c)}\right|^+}{|L^{(c)}|^+}, \tag{19}$$

where the numerator contains measurements from low reconstruction clusters, each of which overlaps with or is adjacent to any clusters. $|\cdot|^+$ represents the number of measurements from specific clusters and "$\cap^+$" means "overlapped with or is adjacent to one or more clusters"

Fig. 16 illustrates our new recall as a function of the allowable separation time between clusters, in hours. Fig. 16 shows the cluster recall of freezing condition is around 70%, which means the observed probability of a freezing cluster being near a low reconstruction cluster is 70%. The cluster recall of direct sunlight condition is around 95%. The cluster recall of precipitation condition increases from 80% to 90% as the allowable separation time increases. These cluster recalls mean that a precipitation cluster or a direct sunlight cluster will most likely be near a low reconstruction cluster.

Finally, the overall cluster recall of low reconstruction condition is over 90%. This means precipitation/surface wetting, freezing condition, and direct sunlight can explain over 90% of the low reconstruction coefficients. We believe the true cluster recall should be higher since there are unrecorded type-2 variations, such as potential precipitation events on 04-12-2018 and 04-14-2018, shown in Figs. 12. Regardless, this shows that the low reconstruction coefficient from the short-term PCA reconstruction is an excellent metric for identifying type-2 variations

Synthetic Damage Detection

This subsection applies the long short-term PCA reconstruction method with a 1-day short-term time window (batch size is $10,000$) and a 10-day long-term time window (batch size is $100,000$) to detect synthetic damage. We calculate the TPR and FPR within these regions by sweeping across a range of thresholds for detecting synthetic damage. From this, we generate the receiver operating characteristics (ROC) curves shown in Fig. 17. Results show that our method achieves an area under the curve (AUC) score of 0.95, 0.91, and 0.80 when the scatter factor is 0.2, 0.1, and 0.05, respectively. An area under the curve of 1.0 represents an ideal detector.

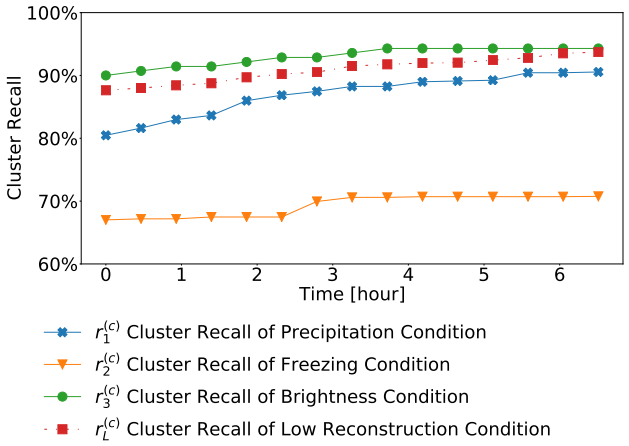

Figure 16. The change of cluster recalls for precipitation, freezing, direct sunlight, and low reconstruction condition with the allowable separation time between clusters. The greater than 90% cluster recall of low reconstruction condition indicates that three type-2 conditions (precipitation, freezing, and direct sunlight) explain over 90% of the low reconstruction of guide waves.

We compare our approach with optimal baseline selection [8,15]. Creating a fair comparison with optimal baseline selection is not straightforward since our approach requires no explicit baseline. Therefore, to make the comparison as fair as possible, we take 100 baselines from the first day of our 30 10-day regions. These baselines do not contain damage and are not significantly affected by sensor drift. When we compute the TPR and FPR, we ignore any measurements with temperature outside one standard from the mean in the baseline data. Hence, we will always have representative baselines. Our detection statistic is then the maximum correlation coefficient among all of the baselines. The ROC curves from these statistics are shown when the scatter factor is 0.2, 0.1 and 0.05, respectively, in Fig. 18. Part of the resulting correlation coefficients are shown in the second plots in Fig. 19, 20, and 21. Missing correlation coefficients are those outside of the baseline temperature range. The results show that optimal baseline selection obtains large false positive rates from type-2 variations, thereby lowering the overall performance.

We illustrate the three sets of short-term and long-term reconstruction coefficients in Fig. 19, 20, and 21, respectively. In each figure, synthetic damage is represented by a grey region of time. In the top plot, the black line illustrates short-term PCA reconstruction and the gray line illustrates long-term PCA reconstruction. The plot highlights long-term reconstruction coefficients that detect damage in orange, based on our damage detection approach, shown in the first subplot.

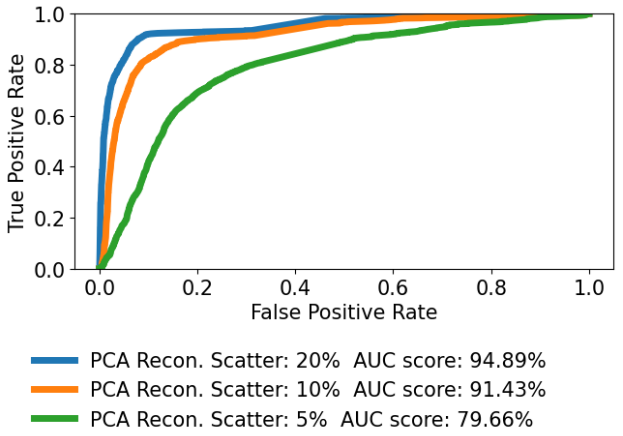

Figure 17. ROC curve and AUC score of synthetic damage detection by the comparison of reconstruction coefficients from the long short-term PCA

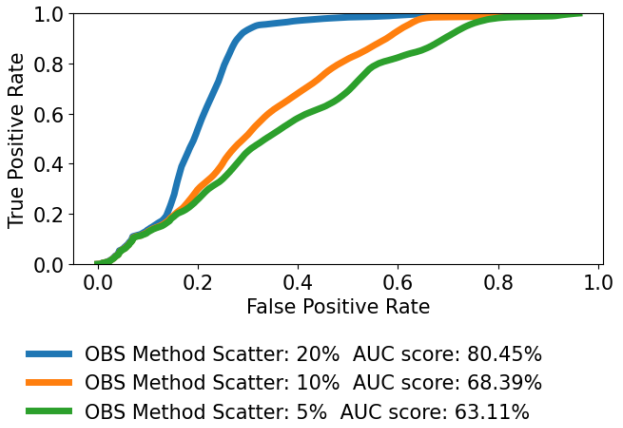

Figure 18. ROC curve and AUC score of synthetic damage detection by the correlation coefficient from optimal baseline selection method (OBS)

In all three figures, both reconstruction coefficients are close to 1 during type-1 variations and drop during precipitation (type-2 variations). During the synthetic damage period, the long-term reconstruction coefficients have a noticeable drop while the short-time reconstruction coefficients remain high. These values fall almost exclusively in the region of synthetic damage. Overall,when setting $\eta = 0.0015$), our method achieves true positive rates of 97.9%, 81.2%, and 75.5% as well as false alarm rates of 1.7%, 2.4%, and 0.0% in Fig. 19, 20, and 21, respectively. There are a small number of spurious drops in long-term reconstruction outside of these regions, such as May 23 and June 25 in Fig. 19 and 20. These false alarms may be related with some type-2 variations since such false alarms are near precipitation and direct sunlight moments.

In contrast, the optimal baseline selection method (when setting the correlation coefficient threshold to 0.975) achieves true positive rates of 97.9%, 81.2%, and 99.4% but with false alarm rates of 19.0%, 61.2%, and 0.0%. in Fig. 19, 20, and 21. Although we have removed correlation coefficients outside of the baseline temperature range, the false positive rates of OBS method are still high. This is

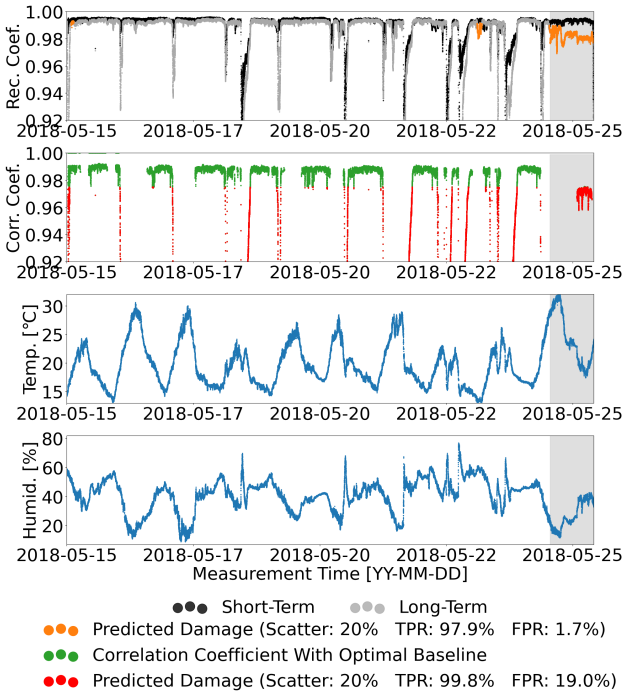

Figure 19. Synthetic damage detection by the comparison of reconstruction coefficients from the short-term PCA and the long-term PCA around precipitation moments

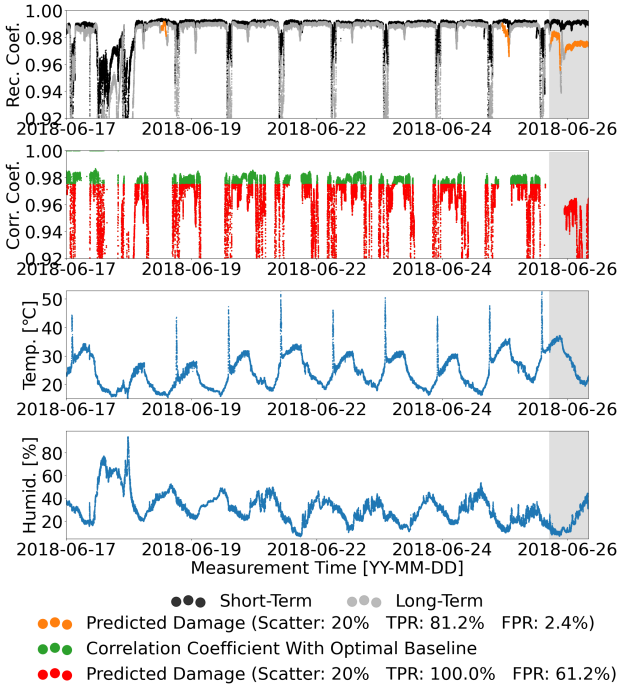

Figure 20. Synthetic damage detection by the comparison of reconstruction coefficients from the short-term PCA and the long-term PCA around direct sunlight moments

due to highly variable environments and deviations from the baselines.

Note that for long-term structural health monitoring, optimal baseline selection has two additional weaknesses. First, for a dataset with approximately seven million measurements, such as described in this work, optimal baseline selection with baseline signal stretch (a current standard approach [8,15]) (with 100 baselines would require

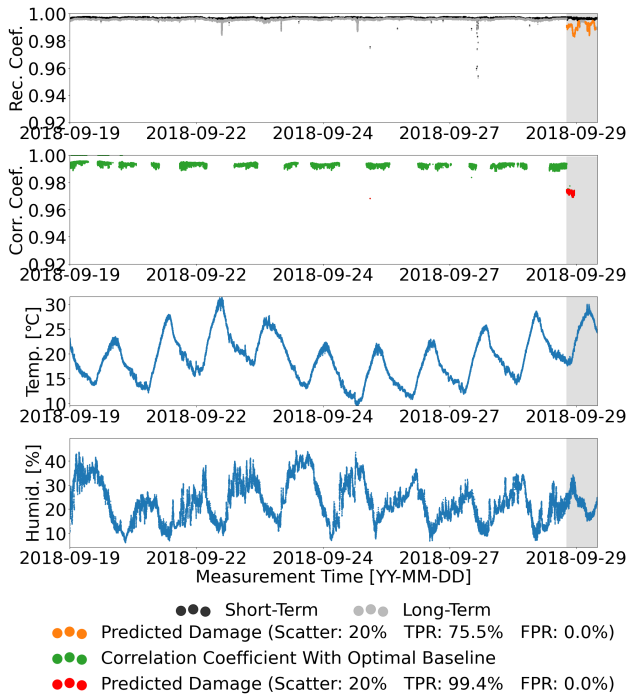

Figure 21. Synthetic damage detection by the comparison of reconstruction coefficients from the short-term PCA and the long-term PCA around fair weather moments.

approximately 4.5 years of computation time (assuming one run of baseline signal stretch requires about 0.2s). Since our approach processes data in batches, the same amount of data requires approximately 10 days of computation time. Second, long-term datasets are plagued by sensor drift, which requires new baselines to be collected over time. In our dataset, for example, two measurements taken at the same temperature but one year apart have a correlation coefficient between each other of approximately 0. We observe small amounts of drift in as little as 10 days. While there have been some efforts to study this[46], there are not yet comprehensive studies.

Overall, the results in Fig 19, 20, and 21 show that our long short-term PCA reconstruction method can detect synthetic damage (type-3/4 variations) under highly variable environments (type-1 and type-2 variations) precisely. The approach is shown to be robust to highly variable conditions of all kinds. In addition, to the knowledge of the authors, no other methods have shown the same resilience to false alarms from type-2 conditions, such as precipitation.

Conclusions

Based on the difference in the reconstruction coefficients obtained from the long-term PCA reconstruction and from the short-term PCA reconstruction, we can identity synthetic damage (type-3/4 variations) from highly variable environments (type-1 and type-2 variations). We identified four categories of type-2 (strong, transient) variations – precipitation, surface wetting, freezing condition, and direct sunlight. When precipitation occurs, reconstruction coefficients will drop, the peak humidity increases, and a drop in temperature and brightness are observed. The surface wetting is observed after precipitation conditions and retains low reconstruction coefficients that slowly increase to 1. Freezing conditions occur when the temperature is close to or below zero degrees Celsius and causes the reconstruction coefficients to decrease below 0.5. Direct sunlight conditions are observed between 10 AM and 11 AM from May to July. Their reconstruction coefficients drop but generally are still above 0.8 and correspond to reductions in humidity. We then showed that we can use this approach to detect type-2 variations to also reduce false alarms caused by them in damage detection.

The main contributions of the paper can be summarized as the following. First, we demonstrated that strong and transient environmental changes cause type-2 variations that cause false alarms. Second, we show that a short-term PCA reconstruction method can classify type-2 variations based on drops in the reconstruction coefficient while remaining nearly invariant to type-1 variations. Third, we show that our long short-term PCA reconstruction method can detect damage under highly variable environments without any prior knowledge. Fourth, we demonstrate the method's performance on classifying type-2 and type-3/4 variations across two years of guided wave data under all kinds of weather.

In future work, we will test our method's performance for detecting realistic, slowly growing damage under highly variable environments. Guided waves from real damage will behave less stationary than synthetic damage. We believe this approach will be able to distinguish these conditions.

Acknowledgements

This material is based upon work supported by the National Science Foundation under grant no. CMMI-1562838 and EECS-1839704.

References

1. Harley JB and Moura JM. Scale transform signal processing for optimal ultrasonic temperature compensation. *IEEE Transactions on Ultrasonics, Ferroelectrics, and Frequency Control* 2012; 59(10): 2226–2236.
2. Cawley P, Lowe M, Alleyne D et al. Practical long range guided wave inspection-applications to pipes and rail. *Materials Evaluation* 2003; 61(1): 66–74.
3. Giurgiutiu V. Lamb wave generation with piezoelectric wafer active sensors for structural health monitoring. In *Smart Structures and Materials 2003: Smart Structures and Integrated Systems*, volume 5056. International Society for Optics and Photonics, pp. 111–122.
4. Ihn JB and Chang FK. Pitch-catch active sensing methods in structural health monitoring for aircraft structures. *Structural Health Monitoring* 2008; 7(1): 5–19.
5. Liu C, Harley JB, Bergés M et al. Robust ultrasonic damage detection under complex environmental conditions using singular value decomposition. *Ultrasonics* 2015; 58: 75–86.
6. Sohn H. Effects of environmental and operational variability on structural health monitoring. *Philosophical Transactions of the Royal Society A: Mathematical, Physical and Engineering Sciences* 2007; 365(1851): 539–560.
7. Konstantinidis G, Wilcox PD and Drinkwater BW. An investigation into the temperature stability of a guided

wave structural health monitoring system using permanently attached sensors. *IEEE Sensors Journal* 2007; 7(5): 905–912.
8. Lu Y and Michaels JE. A methodology for structural health monitoring with diffuse ultrasonic waves in the presence of temperature variations. *Ultrasonics* 2005; 43(9): 717–731.
9. Fallahian M, Khoshnoudian F and Meruane V. Ensemble classification method for structural damage assessment under varying temperature. *Structural Health Monitoring* 2018; 17(4): 747–762.
10. Mariani S, Heinlein S and Cawley P. Compensation for temperature-dependent phase and velocity of guided wave signals in baseline subtraction for structural health monitoring. *Structural Health Monitoring* 2020; 19(1): 26–47.
11. Xu ZD and Wu Z. Simulation of the effect of temperature variation on damage detection in a long-span cable-stayed bridge. *Structural Health Monitoring* 2007; 6(3): 177–189.
12. Moll J and Fritzen CP. Guided waves for autonomous online identification of structural defects under ambient temperature variations. *Journal of Sound and Vibration* 2012; 331(20): 4587–4597.
13. Xia Y, Hao H, Zanardo G et al. Long term vibration monitoring of an rc slab: temperature and humidity effect. *Engineering Structures* 2006; 28(3): 441–452.
14. Liu C, Harley J, O'Donoughue N et al. Ultrasonic monitoring of a pipe under operating conditions. In *Proc. of Sensors and Smart Structures Technologies for Civil, Mechanical, and Aerospace Systems*, volume 8345. International Society for Optics and Photonics, p. 83450B.
15. Konstantinidis G, Drinkwater B and Wilcox P. The temperature stability of guided wave structural health monitoring systems. *Smart Materials and Structures* 2006; 15(4): 967.
16. Croxford AJ, Moll J, Wilcox PD et al. Efficient temperature compensation strategies for guided wave structural health monitoring. *Ultrasonics* 2010; 50(4-5): 517–528.
17. Clarke T, Simonetti F and Cawley P. Guided wave health monitoring of complex structures by sparse array systems: Influence of temperature changes on performance. *Journal of Sound and Vibration* 2010; 329(12): 2306–2322.
18. Meruane V and Heylen W. Structural damage assessment under varying temperature conditions. *Structural Health Monitoring* 2012; 11(3): 345–357.
19. Ren Y, Qiu L, Yuan S et al. Gaussian mixture model–based path-synthesis accumulation imaging of guided wave for damage monitoring of aircraft composite structures under temperature variation. *Structural Health Monitoring* 2019; 18(1): 284–302.
20. Gu J, Gul M and Wu X. Damage detection under varying temperature using artificial neural networks. *Structural Control and Health Monitoring* 2017; 24(11): e1998.
21. Benn J. Railway bridge failure during flooding in the uk and ireland. *Proceedings of the Institution of Civil Engineers-Forensic Engineering* 2013; 166(4): 163–170.
22. Kozmar H, Procino L, Borsani A et al. Sheltering efficiency of wind barriers on bridges. *Journal of Wind Engineering and Industrial Aerodynamics* 2012; 107: 274–284.
23. Li Z, Chan TH and Ko JM. Fatigue damage model for bridge under traffic loading: application made to tsing ma bridge. *Theoretical and Applied Fracture Mechanics* 2001; 35(1): 81–91.
24. Parent O and Ilinca A. Anti-icing and de-icing techniques for wind turbines: Critical review. *Cold Regions Science and Technology* 2011; 65(1): 88–96.
25. Gao H and Rose JL. Ice detection and classification on an aircraft wing with ultrasonic shear horizontal guided waves. *IEEE Transactions on Ultrasonics, Ferroelectrics, and Frequency control* 2009; 56(2): 334–344.
26. Carden EP and Fanning P. Vibration based condition monitoring: a review. *Structural Health Monitoring* 2004; 3(4): 355–377.
27. Fan W and Qiao P. Vibration-based damage identification methods: a review and comparative study. *Structural Health Monitoring* 2011; 10(1): 83–111.
28. Das S, Saha P and Patro S. Vibration-based damage detection techniques used for health monitoring of structures: a review. *Journal of Civil Structural Health Monitoring* 2016; 6(3): 477–507.
29. Sarrafi A, Mao Z, Niezrecki C et al. Vibration-based damage detection in wind turbine blades using phase-based motion estimation and motion magnification. *Journal of Sound and vibration* 2018; 421: 300–318.
30. Lang ZQ, Park G, Farrar CR et al. Transmissibility of non-linear output frequency response functions with application in detection and location of damage in mdof structural systems. *International Journal of Non-Linear Mechanics* 2011; 46(6): 841–853.
31. Abdeljaber O, Avci O, Kiranyaz S et al. Real-time vibration-based structural damage detection using one-dimensional convolutional neural networks. *Journal of Sound and Vibration* 2017; 388: 154–170.
32. Padil KH, Bakhary N and Hao H. The use of a non-probabilistic artificial neural network to consider uncertainties in vibration-based-damage detection. *Mechanical Systems and Signal Processing* 2017; 83: 194–209.
33. Kang F, Li JJ and Xu Q. Damage detection based on improved particle swarm optimization using vibration data. *Applied Soft Computing* 2012; 12(8): 2329–2335.
34. Mujica L, Rodellar J, Fernandez A et al. Q-statistic and t2-statistic pca-based measures for damage assessment in structures. *Structural Health Monitoring* 2011; 10(5): 539–553.
35. Yin T, Jiang QH and Yuen KV. Vibration-based damage detection for structural connections using incomplete modal data by bayesian approach and model reduction technique. *Engineering Structures* 2017; 132: 260–277.
36. Figueiredo E, Park G, Farrar CR et al. Machine learning algorithms for damage detection under operational and environmental variability. *Structural Health Monitoring* 2011; 10(6): 559–572.
37. O'Brien E, Carey C and Keenahan J. Bridge damage detection using ambient traffic and moving force identification. *Structural Control and Health Monitoring* 2015; 22(12): 1396–1407.
38. Tong G, Aiqun L and Jianhui L. Fatigue life prediction of welded joints in orthotropic steel decks considering temperature effect and increasing traffic flow. *Structural Health Monitoring* 2008; 7(3): 189–202.
39. Jesus A, Brommer P, Westgate R et al. Bayesian structural identification of a long suspension bridge considering temperature and traffic load effects. *Structural Health Monitoring* 2019; 18(4): 1310–1323.
40. Li H, Li S, Ou J et al. Modal identification of bridges under varying environmental conditions: temperature and wind

effects. *Structural Control and Health Monitoring* 2010; 17(5): 495–512.

41. Comanducci G, Magalhães F, Ubertini F et al. On vibration-based damage detection by multivariate statistical techniques: Application to a long-span arch bridge. *Structural Health Monitoring* 2016; 15(5): 505–524.
42. Kim S, Adams DO and Harley JB. A study of environmental effects on long term guided wave structural health monitoring in outdoor conditions. *In Proc of Review of Progress in Quantitative Nondestructive Evaluation* 2019; .
43. Kim S, Shiveley S, Douglass ACS et al. Efficient storage and processing of large guided wave data sets with random projections. *Structural Health Monitoring* 2020; : 1475921720960196.
44. Harley JB and Chia CC. Statistical partial wavefield imaging using lamb wave signals. *Structural Health Monitoring* 2018; 17(4): 919–935.
45. Weather Underground. Salt Lake City, UT Weather History. URL `https://www.wunderground.com/history/daily/us/ut/salt-lake-city`.
46. Attarian VA, Cegla FB and Cawley P. Long-term stability of guided wave structural health monitoring using distributed adhesively bonded piezoelectric transducers. *Structural Health Monitoring* 2014; 13(3): 265–280.